Inferring prompt black-hole formation in neutron star mergers from gravitational-wave data

Michalis Agathos[1,2,3,*] Francesco Zappa[1], Sebastiano Bernuzzi[1], Albino Perego[4,5]
Matteo Breschi[1], and David Radice[6,7,8,9]

[1]*Theoretisch-Physikalisches Institut, Friedrich-Schiller-Universität Jena, 07743, Jena, Germany*
[2]*DAMTP, University of Cambridge, Wilberforce Road CB3 0WA, Cambridge, United Kingdom*
[3]*Kavli Institute for Cosmology, University of Cambridge, Madingley Road CB3 0HA,
Cambridge, United Kingdom*
[4]*Dipartimento di Fisica, Universitá di Trento, Via Sommarive 14, 38123 Trento, Italy*
[5]*Istituto Nazionale di Fisica Nucleare, Sezione di Milano-Bicocca,
Piazza della Scienza 20100, Milano, Italy*
[6]*Department of Physics, The Pennsylvania State University, University Park, Pennsylvania 16802, USA*
[7]*Department of Astronomy and Astrophysics, The Pennsylvania State University,
University Park, Pennsylvania 16802, USA*
[8]*Institute for Advanced Study, 1 Einstein Drive, Princeton, New Jersey 08540, USA*
[9]*Department of Astrophysical Sciences, Princeton University,
4 Ivy Lane, Princeton, New Jersey 08544, USA*

The gravitational wave GW170817 is associated with the inspiral phase of a binary neutron star coalescence event. The LIGO-Virgo detectors' sensitivity at high frequencies was not sufficient to detect the signal corresponding to the merger and postmerger phases. Hence, the question whether the merger outcome was a prompt black-hole formation or not must be answered using either the premerger gravitational-wave signal or electromagnetic counterparts. In this work we present two methods to infer the probability of prompt black-hole formation, using the analysis of the inspiral gravitational-wave signal. Both methods combine the posterior distribution from the gravitational-wave data analysis with numerical-relativity results. One method relies on the use of phenomenological models for the equation of state and on the estimate of the collapse threshold mass. The other is based on the estimate of the tidal polarizability parameter $\tilde{\Lambda}$ that is correlated in an equation-of-state agnostic way with the prompt black-hole formation. We analyze GW170817 data and find that the two methods consistently predict a probability of $\sim$50%–70% for prompt black-hole formation, which however may significantly decrease below 10% if the maximum mass constraint from PSR J0348+0432 or PSR J0740+6620 is imposed.

I. INTRODUCTION

The gravitational-wave (GW) signal GW170817, detected by the LIGO-Virgo detector network [1,2], is a chirp transient compatible with the emission from a binary neutron star (NS) system coalescence in the late-inspiral phase [3–5]. The signal has a significant signal-to-noise ratio (SNR) in the range 30–600 Hz, roughly corresponding to the last 1300–10 orbits to merger for an equal-mass binary with total mass $M \sim 2.7$ $M_\odot$. The data analysis of GW170817 provided us with an estimate of the dominant tidal polarizability parameter that, in turn, constrains the NS cold equation of state [6–10]. The LIGO-Virgo detectors' sensitivity was not sufficient to detect a signal from the merger phase and the remnant, which lie in the kilohertz range [11]. An outstanding question is thus whether the coalescence resulted in the formation of a black hole (BH) or in a NS remnant.

A first answer was given by the interpretation of the electromagnetic (EM) counterparts observed with delays of seconds to days with respect to the GW and composed by a gamma-ray burst [12–14] and a kilonova [15–20]. The energetics and timing of the latter exclude both a prompt BH formation and a long-lived remnant, e.g., [21,22]. Most likely, the merger dynamics produced a hypermassive NS that collapsed on timescales of $\sim$0.01 to $\sim$2 s. Such a conclusion is informed and supported by numerical-relativity (NR) results that established the formation of hypermassive NS remnants for canonical NS masses and equations of state supporting $M_{\mathrm{TOV}}^{\max} \gtrsim 2$ $M_\odot$ [22–30].

In this work, we explore a different approach to inferring the merger remnant. Instead of considering the EM

*magathos@damtp.cam.ac.uk

044006-1

counterparts, we consider the premerger GW and infer binary parameters using the late-inspiral solely. The posterior distributions of these parameters are then combined with information from NR simulations. Our methods allow us to quantify the probability that a BH was promptly formed.

This paper is structured as follows: Sec. II outlines the input from NR data in our inference methods, based on which we classify the outcome of a binary neutron star (BNS) merger; the two methods are introduced in Sec. III and are validated by analyzing a set of simulated GW detections in Sec. IV; we perform the analysis on GW170817 data and present our results in Sec. V, while some concluding remarks are given in Sec. VI. We use geometric units $G = c = 1$ unless stated differently.

II. PROMPT-COLLAPSE THRESHOLD

A. Mass threshold estimate

Numerical-relativity simulations indicate that a NS binary merger will be followed by a prompt collapse to a BH, if the total gravitational mass M of the binary exceeds a threshold mass, given by [27,28]

$$M_{\text{thr}} = k_{\text{thr}} M_{\text{TOV}}^{\max}. \tag{1}$$

In the expression above, k_{thr} depends, in general, on the equation of state (EOS), mass ratio, and spin, while $M_{\text{TOV}}^{\max}$ is the gravitational mass of the heaviest stable nonrotating NS, which also depends on the EOS. Empirically, the prompt-collapse threshold is calculated from the simulations by considering remnants that collapse within 2 ms from the waveform peak amplitude (conventionally, the "merger time"). Examples of merger waveforms for a prompt collapse and a NS remnant are shown in Fig. 1.
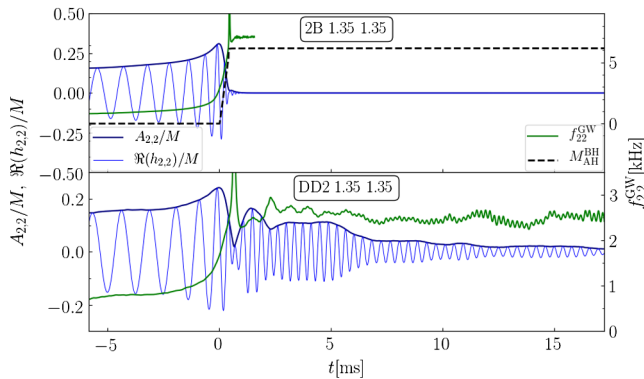

FIG. 1.   Example of waveforms for a binary neutron star merger for two different EOS but same component NS masses $M_A = M_B = 1.35 \, M_\odot$. Upper panel: Prompt collapse occurs after collision; the waveform amplitude drops to 0 while an apparent horizon (dashed black line) originates within 2 ms from the waveform peak amplitude. Bottom panel: A stable massive NS remnant forms.

In the prompt-collapse case an apparent horizon forms during the simulation at a time close to the retarded merger time; the waveform frequency at those times corresponds to the quasinormal mode of the black hole.

For a sample of hadronic EOS and equal-mass nonspinning binaries, the threshold coefficient in Eq. (1) is found in the range [27,28,31]

$$1.3 \lesssim k_{\text{thr}} \lesssim 1.7. \tag{2}$$

Considering a sample of equal-mass, nonspinning binaries and 12 hadronic EOS, Ref. [28] showed that k_{thr} has an approximately EOS-independent linear behavior in the maximum compactness $C_{\max}$ of nonrotating equilibrium NS solution. Note that by inverting Eq. (1) and *assuming* that the merger did not promptly form a BH, one may obtain a bound on the maximum stable NS mass [22,32,33].

We have repeated the analysis on the threshold mass with the data of CORE Collaboration [34,35] by including ten new simulations with five EOS and different masses and spins. We have compared and combined our new results with the ones reported in [27,28,31]. Our final sample includes 18 different hadronic EOS and for eight of them results from more than one analysis are available. Using the results reported by [28,31], and by adding the data of CORE Collaboration, we find a linear fit with updated coefficients that reads

$$k_{\text{thr}}(C_{\max}) = -(3.29 \pm 0.23)C_{\max} + (2.392 \pm 0.064). \tag{3}$$

The data that were used for this fit are given in the Appendix A, along with further details.

B. Tidal parameter threshold estimate

Alternatively, the prompt-collapse threshold can be characterized in an EOS-independent way in terms of the tidal polarizability parameter

$$\kappa_2^T = \frac{3}{2}[\Lambda_2^A X_A^4 X_B + \Lambda_2^B X_B^4 X_A], \tag{4}$$

where the tidal polarizability coefficient of star A is

$$\Lambda_2^A = \frac{2}{3} k_2^A \left(\frac{c^2}{G} \frac{R_A}{M_A} \right)^5 \tag{5}$$

and k_2^A is the quadrupolar gravito-electric Love number [36–38]. Above, (R_A, M_A) are the NS areal radius and mass, respectively, and $X_A = M_A/M$. The Λ_2 parameter is strongly dependent on the NS internal structure; thus, its measurement provides a constraint on the NS EOS.[1] The binary's post-Newtonian tidal dynamics and waveform are

_____

[1]Black holes are not deformed in this way; black-hole static perturbations lead to $k_2 = 0$ [38–41].

parametrized at leading order by κ_2^T [6,42]. A tidal polarizability parameter commonly used in GW analysis (and equivalent to κ_2^T for equal-mass binaries) is

$$\tilde{\Lambda} = \frac{16}{13} \frac{(M_A + 12 M_B) M_A^4}{M^5} \Lambda_A + (A \leftrightarrow B). \qquad (6)$$

By analyzing the NR data of the CORE Collaboration, Ref. [34] found that all the reported prompt-collapse mergers are captured by the condition $\kappa_2^T < 73$, with a variability of $\delta\kappa_2^T < 40$, depending on the EOS. Inspection of the same NR data provided also a range for the value of $\tilde{\Lambda}$ at the prompt-collapse threshold:

$$338 \lesssim \tilde{\Lambda}_{\text{thr}} \lesssim 386. \qquad (7)$$

III. METHOD

Based on the universal behavior discussed in Sec. II, we present two different ways of inferring whether a BNS merger is followed by a prompt collapse to a BH using solely GW data (with the exception of the sky location which we may fix to the one obtained by EM observations, when an EM counterpart is available). We test the validity of our methods against a set of high-resolution numerical simulations of BNS mergers with different masses and EOS.

For our Bayesian data analysis on the GW signal, we use a Markov-chain Monte Carlo (MCMC) algorithm as implemented in the LALInference software package [43], with a setup similar to the one employed in the latest LIGO-Virgo Collaboration (LVC) analysis of GW170817 [4,10].

A. Threshold mass

For this method we make use of the mass threshold estimate of Sec. II A, whereby the total mass M of the progenitor NS binary being larger or smaller than M_{thr} determines whether the product of the merger will promptly collapse to a BH or not. The threshold mass M_{thr} depends on the EOS via Eqs. (1) and (3). We perform a full Bayesian analysis on the data, that returns posterior distributions for the binary parameters, including the EOS. The barotropic EOS for the cold dense NS matter is sampled through a four-dimensional family of pressure-density functions $P(\rho)$, parametrized by $(\gamma_0, \gamma_1, \gamma_2, \gamma_3)$ in the spectral decomposition [10,44,45], a smooth alternative to piecewise polytropic models [9,46], where the adiabatic index $\Gamma = \rho \frac{d \ln P}{d\rho}$ is given by

$$\Gamma = \exp\left[\sum_{k=0}^{3} \gamma_k \log(p/p_0)^k\right], \qquad (8)$$

with p_0 some reference pressure. For each sampled point in the parameter space, we solve the Tolman-Oppenheimer-Volkoff (TOV) equations to calculate not only the tidal polarizability parameters Λ_2^A which are used to model the

tidal effects in the waveform, but also the values for $M_{\text{TOV}}^{\text{max}}$, C_{max} and k_{thr}. We can thus translate the joint posterior probability density function (PDF) on masses and EOS parameters $(M_A, M_B, \gamma_0, \gamma_1, \gamma_2, \gamma_3)$ into a joint posterior PDF on the (M, M_{thr}) plane. The fraction of the posterior distribution that lies above the diagonal is equal to the posterior probability of prompt collapse

$$P_{\text{PC}} = P(M > M_{\text{thr}}(\vec{\gamma})|d), \qquad (9)$$

where $\vec{\gamma} = (\gamma_0, \gamma_1, \gamma_2, \gamma_3)$ and d denotes our data.

As an additional step, one may choose to impose further implicit constraints on the parameter space, such as requiring that the EOS support NS masses larger than a given value, for instance, the observation of the binary pulsar PSR J0348+0432 [47] and the narrow measurement of the pulsar's mass, or even the more recent measurement of an even heavier (but with larger uncertainty) pulsar mass in J0740+6620 [48]. In one of the analyses of [10] the conservative 1σ bound for PSR J0348+0432 at 1.97 $M_\odot$ was considered as a hard constraint. Here we take a different approach and marginalize over the mass measurement uncertainties into our analysis by treating that measurement as a random variable sampled from a normal distribution that is adapted to the mean and standard deviation of the measurement and weighing the posterior samples accordingly.

B. Threshold tidal parameter

For the second method we again employ a Bayesian analysis of the GW data, this time focusing on the posterior distribution of the tidal deformability parameter $\tilde{\Lambda}$ given by Eq. (6). The setup of our Bayesian analysis follows that of [4]. We then make use of the corresponding criterion of Eq. (7) in order to estimate the probability of prompt collapse. Note that the criterion defines a transition region between the studied cases where the merger product undergoes prompt collapse and the ones where it does not. The outcomes of NR simulations within this transition region are not perfectly ordered. We treat this classification problem by assigning a probability distribution to the uncertainty of the threshold value $\tilde{\Lambda}_{\text{thr}}$ instead of choosing a hard threshold or, equivalently, by defining a sigmoid-type conditional probability of prompt collapse for a given value of $\tilde{\Lambda}$ as

$$P(\text{prompt collapse}|\tilde{\Lambda}) = \frac{1}{1 + e^{\frac{\tilde{\Lambda} - \tilde{\Lambda}_0}{\beta}}}, \qquad (10)$$

which tends to 1 (0) for small (large) values of $\tilde{\Lambda}$. The values for the sigmoid parameters, i.e., the central value and the width, are chosen based on the available set of NR simulations in this region to be $\tilde{\Lambda}_0 \approx 362$ and $\beta \approx 13.7$, respectively. Then, once the posterior PDF $p(\tilde{\Lambda}|d)$ is

TABLE I. Summary of injections and `TaylorF2` recovery. Collapse time t_{BH} is reported from merger time, defined at the peak of the amplitude. We indicate with HMNS (MNS) remnants that are short (long) lived, i.e., that (do not) collapse to a BH within the simulated time. All the simulations are performed at standard resolution of Ref. [50]. The last three columns give the inferred probabilities of prompt collapse based on the threshold-mass method (with and without the constraint $M_{TOV}^{max} > 1.97\ M_\odot$) and the threshold-$\tilde\Lambda$ method. Because for 2B the heaviest NS is lighter than the M_{TOV}^{max} constraint, we mark the corresponding result with an asterisk, indicating that the injected model lies outside our prior range.

EOS	M_{TOV}^{max} [$M_\odot$]	C_{max}	M_{thr} [$M_\odot$]	M_A [$M_\odot$]	M_B [$M_\odot$]	$\mathcal{M}_c$ [$M_\odot$]	Λ_2^A	Λ_2^B	$\tilde\Lambda$	t_{BH} [ms]	Remnant at $t \sim 3$ ms	Ref.	$P_{PC}^{M_{thr}}$ %	$P_{PC}^{M_{thr},M_{TOV}^{max}}$ %	$P_{PC}^{\tilde\Lambda_{thr}}$ %
2B	1.78	0.3120	$2.43_{-0.24}^{+0.24}$	1.35	1.35	1.17	127	127	127	0.49	BH	[51]	99.5	48.3*	100
SLy	2.06	0.3066	$2.87_{-0.30}^{+0.26}$	1.50	1.50	1.30	191	191	191	0.99	BH	[35]	94.5	82.9	100
LS220	2.04	0.2841	$2.95_{-0.24}^{+0.29}$	1.60	1.60	1.39	202	202	202	0.63	BH	[30,50,52]	90.0	84.4	99.9
SFHo	2.06	0.2952	$2.95_{-0.29}^{+0.25}$	1.46	1.46	1.27	252	252	252	0.70	BH	[30,50,52]	72.7	40.4	97.8
BHB$\Lambda\phi$	2.11	0.2677	$3.10_{-0.18}^{+0.35}$	1.60	1.60	1.39	306	306	306	0.99	BH	[30,50,52,53]	36.0	19.6	72.9
DD2	2.42	0.3007	$3.35_{-0.28}^{+0.37}$	1.59	1.59	1.38	332	332	332	~ 3	BH	[53]	32.1	18.5	66.2
SFHo	2.06	0.2952	$2.95_{-0.29}^{+0.25}$	1.40	1.40	1.22	334	334	334	1.07	BH	[30,52]	41.7	4.9	60.6
ALF2	1.99	0.2602	$2.87_{-0.06}^{+0.43}$	1.50	1.50	1.30	382	382	382	0.64	BH	[35]	20.9	3.6	29.2
SLy-SOR	2.06	0.3066	$2.87_{-0.30}^{+0.26}$	1.34	1.34	1.17	401	401	401	~ 14	HMNS	This work	25.0	0.4	21.8
SLy-SOR	2.06	0.3066	$2.87_{-0.30}^{+0.26}$	1.43	1.26	1.17	264	592	401	~ 13	HMNS	This work	23.7	0.1	21.6
SFHo	2.06	0.2952	$2.95_{-0.29}^{+0.25}$	1.44	1.27	1.18	274	606	412	~ 12	HMNS	This work	21.6	2.0	17
SFHo	2.06	0.2952	$2.95_{-0.29}^{+0.25}$	1.35	1.35	1.18	413	413	413	~ 4	HMNS	[30,50,52]	20.5	0.2	15.6
LS220	2.04	0.2841	$2.95_{-0.24}^{+0.29}$	1.44	1.25	1.17	432	1136	713	~ 33	HMNS	This work	2.4	0.0	0
LS220	2.04	0.2841	$2.95_{-0.24}^{+0.29}$	1.34	1.34	1.17	715	715	715	~ 16	HMNS	This work	0.7	0.0	0
DD2	2.42	0.3007	$3.35_{-0.28}^{+0.37}$	1.36	1.36	1.18	840	840	840	~ 21	MNS	[54]	0.1	0.0	0
DD2	2.42	0.3007	$3.35_{-0.28}^{+0.37}$	1.24	1.24	1.08	1366	1366	1366	> 20	MNS	[30]	0.0	0.0	0
BHB$\Lambda\phi$	2.11	0.2677	$3.10_{-0.18}^{+0.35}$	1.24	1.24	1.08	1367	1367	1367	> 20	MNS	[53]	0.0	0.0	0

calculated, the probability of prompt collapse is simply computed by integrating the posteriors from the minimum value up to the threshold value using the sigmoid of Eq. (10) as a kernel:

$$P_{PC} = \int d\tilde\Lambda\ P(\text{prompt collapse}|\tilde\Lambda) p(\tilde\Lambda|d). \quad (11)$$

Note that this method does not rely on any assumption about the EOS, but only on the phenomenological parameter $\tilde\Lambda$ which is directly measured from the data. In the present analysis we assume that Eq. (7) holds independently on q and spins. That hypothesis is justified by inspection of the CORE data that span $q \in [1, 2]$ and dimensionless spins up to ~ 0.1.[2]

---

[2] Recently, Ref. [49] demonstrated a set of targeted numerical simulations with a selection of piecewise polytropic EOS, among which one case results in a prompt BH formation with $\tilde\Lambda$ as low as 242. The pressures met in this asymmetric BNS lie at the very edge (beyond 99%) of our prior, possibly due to the extreme choice of the thermal component ($\Gamma_{th} = 1.8$). Thus, taking the trial factor into account, this result is not at odds with our probabilistic predictions.

IV. INJECTION STUDIES

We validate our methods using injections of known inspiral-merger waveforms corresponding to binaries simulated in NR. We demonstrate that both methods are effective in estimating the collapse threshold and study their systematics.

A. Setup

We consider NR merger simulations of irrotational binaries with different chirp masses specifically performed for this work together with data previously presented in [30,35,50–54]. The new simulations are performed with the WhiskyTHC code [55–57] at multiple grid resolutions, using the same setup described in [30,50,52].

The main properties of the simulated binaries, the outcome of the merger and the summary data from the injection are summarized in Table I. We simulate with five microphysical EOS: the BHB$\Lambda\phi$ EOS [58], the DD2 EOS [59,60], the LS220 EOS [61], the SFHo EOS [62], the SLy-SOR EOS [63]; and three piecewise polytropic: the ALF2, 2B and the SLy EOS [46]. The microphysical EOS predict NS maximum masses and radii within the range allowed by current astrophysical constraints. The 2B EOS is representative of soft EOS that do not support the largest NS masses
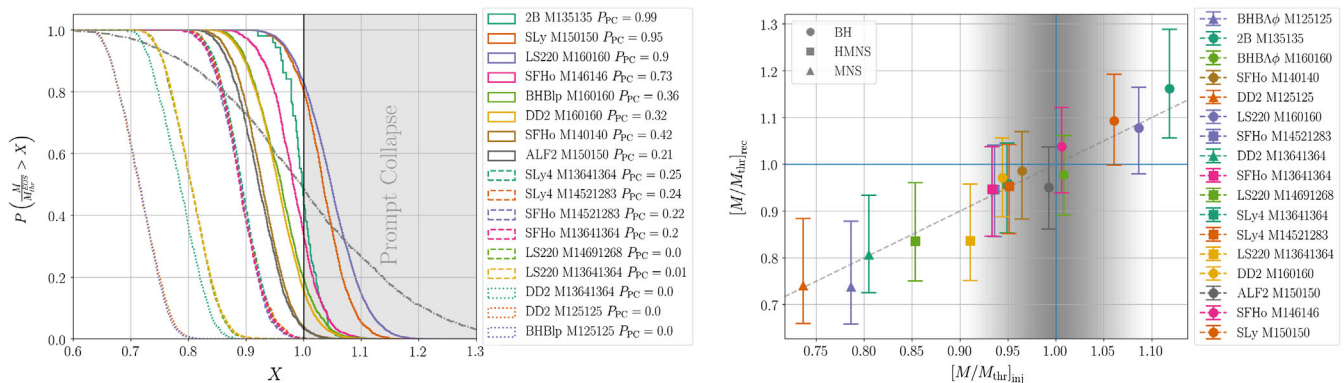
FIG. 2.   Results of the injection study, for the threshold-mass method using the simulated BNS events of Table I. Left: Cumulative probability of M/M_{thr}, the ratio between total mass and threshold mass. The inferred probability of prompt collapse for each BNS event is the value of its curve at $X = 1$. Solid, dashed and dotted lines indicate a BH, HMNS and MNS remnant, respectively. To illustrate how informative the data are, the prior is shown in the gray dash-dotted line. Right: Summary of the injected values of M/M_{thr} versus the recovered median values and 90% confidence intervals, for the simulated BNS events. Circles, squares and triangles indicate a BH, HMNS and MNS remnant, respectively (from NR). The threshold uncertainty due to the error in the fitting formula of Eq. (3) is shown as the gray shaded band.

observed so far [47,48]. All the simulations with chirp mass $\mathcal{M}_c \sim 1.18\ M_\odot$ and tidal deformability compatible with GW170817 except 2B predict a short-lived NS remnant collapsing to BH within ~ 15 ms. The simulation DD2 $1.59 + 1.59$ with $\tilde{\Lambda} = 332$ is below the $\tilde{\Lambda}$ threshold for prompt BH formation but forms a short-lived NS with lifetime ~ 3 ms [53]. While this is possibly related to numerical uncertainties, the binary provides an interest borderline case.

Throughout this work we use the terms hypermassive NS (HMNS) and massive NS (MNS) with a slightly different meaning than what is commonly used in the literature.[3] We indicate with HMNS (MNS) merger remnants that are short (long) lived, i.e., that (do not) collapse to a BH within the simulated time. The reason for this choice is that merger remnants are not cold equilibrium NS configurations, and their secular evolution is far from being understood (see e.g., discussion in [30].)

The simulations provide us with dynamics and waveform starting from GW frequencies ~ 500–900 Hz, depending on the binary mass and simulation length. Hence, the NR waveforms alone are not sufficient to perform the injection of BNS signals. Waveforms spanning from an initial GW frequency of 30 Hz to merger and corresponding to the binaries of Table I are constructed with the TEOBResumS waveform model [51,66]. Specifically, we use the non-spinning tidal model of [67] with gravitational-self-force resummed gravitoelectric and post-Newtonian gravito-magnetic terms (Model GSF23$^{(+)}$PN$^{(-)}$ with $p = 4$ of

Table I in [67]). Waveforms are generated using the postadiabatic inspiral speed-up developed in [68].[4]

For our Bayesian data analysis on the simulated GW signals, we use a MCMC algorithm as implemented in the LALInference software package [43,70], with a setup similar to the one employed in the latest LVC analysis of GW170817 [4,10]. The simulated signals are coherently projected and analyzed as the output strain of LIGO Hanford (H1), LIGO Livingston (L1) and Virgo (V1) at design sensitivity. The intrinsic parameters of the non-spinning BNS sources are given in Table I, while the location and orientation parameters are compatible with GW170817. In order to isolate possible systematics from statistical uncertainties due to noise, we perform our tests on the zero-noise realization.

We perform our analyses using two differ-ent waveform models, namely TaylorF2 and IMRPhenomPv2NRtidal, both restricted to aligned dimensionless spins ranging within $[-0.05, 0.05]$ (the low-spin prior of [4]). The tidal effects are modeled in the case of TaylorF2 up to 2.5PN beyond leading order [6] and in the case of IMRPhenomPv2 using the NRTidal approach of [71].

In the threshold-mass method, we are able to additionally impose an observational constraint on the EOS prior, coming from the heaviest observed NS. This can be either a hard constraint at a chosen mass value (e.g., $1.97\ M_\odot$ as in [10]) or a probabilistic constraint that takes into account the measured posterior PDF. In the latter case we will use the median and 1σ error of the mass measurement of PSR J0348+0432 [47] to reconstruct a Gaussian PDF for the heaviest observed NS mass

---

[3]A HMNS is defined as a differentially rotating NS at equilibrium with mass above the uniformly rotating limit [64]. A supramassive NS is a rotating NS at equilibrium with rest mass exceeding the nonrotating limit M_{TOV}^{max} [65]. A remnant with mass below M_{TOV}^{max} is usually indicated as MNS.

[4]The public available TEOBResumS code can be found at Ref. [69].

$p(\overline{M}_{\max}) = \mathcal{N}(2.01\ M_\odot, 0.04\ M_\odot)$ and assign a weight w on each sampled EOS appropriately, according to its maximum NS mass,

$$w(\vec{\gamma}) = p(M_{\mathrm{TOV}}^{\max}(\vec{\gamma}) > \overline{M}_{\max}). \tag{12}$$

A comparison between results derived with and without such a constraint is demonstrated in Appendix C.

B. Results

We find that the `IMRPhenomPv2NRtidal` waveform systematically underestimates the inference of the injected $\tilde{\Lambda}$. This result was anticipated by the high SNR injections of [72,73] but could not be studied systematically due to the limited number of injections performed there. A similar bias is present in the EOS inference runs with `IMRPhenomPv2NRtidal`, but the mass threshold method to determine the prompt collapse is less affected by systematics on tidal parameters than the $\tilde{\Lambda}$ threshold method. In the following, we discuss only the results obtained with `TaylorF2`. The effect of waveform systematics on the results is discussed in Appendix B; a full account of the waveform's systematics in these injection experiments will be given elsewhere.

The recovery results with `TaylorF2` are summarized in Table I. Results from the threshold-mass analysis with maximum mass constrained to be larger than the mass of PSR J0348+0432 are also shown in Fig. 2 [see Appendix C for a similar plot without the maximum mass constraint]. The left panel shows for each injection the cumulative probability distribution to find $M > M_{\mathrm{thr}}$; the vertical line marks the collapse threshold. The right panel shows for each injection the inferred mass divided by the inferred threshold mass $[M/M_{\mathrm{thr}}]_{\mathrm{rec}}$ versus the same injected quantity, $[M/M_{\mathrm{thr}}]_{\mathrm{inj}}$. Erroneous recoveries would populate the top-left and bottom-right quadrants of the plot. The plot

shows that the inference returns the correct estimate of the prompt collapse for the majority of the injections. SFHo $1.46 + 1.46$ is a borderline case for which $P_{\mathrm{PC}} \sim 40\%$. However, we observe that a few simulations that led to a prompt collapse (denoted by solid lines and circles in the plots) were not recovered as such. This misclassification had occurred already at the level of injection parameters, since their position on the x axis (right panel) lies below unity, which is due to the inherent uncertainty on the estimation of k_{thr} from fitting NR data. The resulting error is comparable in size to the statistical error of our parameter estimation.

Results from the threshold tidal parameter analysis are shown in Fig. 3. The left panel shows for each injection the probability that $\tilde{\Lambda}$ is smaller than a given value. The latter should be compared to Eq. (10), shown as a black solid line. The right panel summarizes the inference results in a way analogous to Fig. 2. The threshold tidal parameter analysis incorrectly predicts few cases for BNS with $\tilde{\Lambda} \sim \tilde{\Lambda}_{\mathrm{thr}}$. SFHo $1.40 + 1.40$ ($\tilde{\Lambda} = 334$) and ALF2 $1.50 + 1.50$ ($\tilde{\Lambda} = 382$) are predicted with 61% and 29% probability, respectively, of producing a NS remnant while the simulations indicate prompt BH formation. The two SLy-SOR binaries ($\tilde{\Lambda} \sim 401$) are predicted with $\sim 22\%$ probability of prompt collapse while the merger produces a HMNS. DD2 $1.59 + 1.59$ ($\tilde{\Lambda} = 332$) is predicted to promptly form a BH with 66% probability, with the simulation resulting in a HMNS of very short life of ~ 3 ms.

We conclude that both methods infer correctly the merger outcome of the simulations, except for a few cases corresponding to BNS close to the collapse threshold. Excluding these cases (in which the answer given is anyway inconclusive), the mass threshold analysis with the maximum mass constraint better captures the formation of a NS remnant, while the threshold $\tilde{\Lambda}$ analysis captures more robustly the prompt-collapse cases. The mass threshold analysis without the maximum mass constraint gives
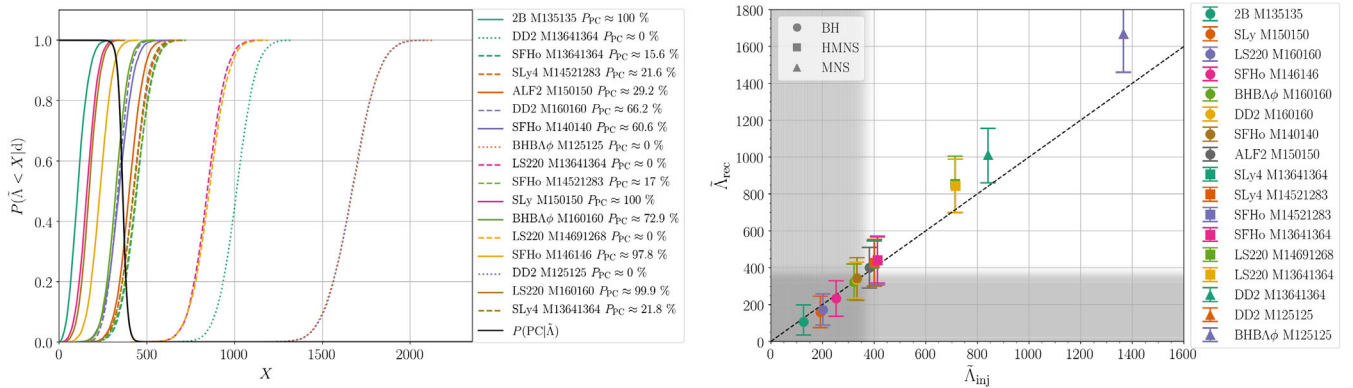

FIG. 3.　Results of the injection study, for the threshold-$\tilde{\Lambda}$ method using the simulated BNS events of Table I. Left: Cumulative probability of $\tilde{\Lambda}$ and the inferred probability of prompt collapse for each event. Solid, dashed and dotted lines indicate a BH, HMNS and MNS remnant, respectively. The solid black line corresponds to the prior probability of prompt collapse as a function of $\tilde{\Lambda}$ [Eq. (10)]. Right: Summary of injected values of $\tilde{\Lambda}$ versus recovered median values and 90% confidence intervals, for the simulated BNS events. Circles, squares and triangles indicate a BH, HMNS and MNS remnant, respectively (from NR).

instead results comparable to the threshold $\tilde{\Lambda}$ analysis. This can be understood by inspecting the EOS posteriors in Appendix D. The EOS inference from the inspiral data constrains more strongly the EOS at densities comparable to the maximum density of the individual NS in the binary. These densities are those that determine the individual masses and thus the Λ_A parameters. Introducing a maximum mass constraint effectively corresponds to introducing a lower bound on the mass distribution of the individual NS (and on k_{thr}), thus lowering the collapse probability.

V. APPLICATION TO GW170817

We apply our analysis methods to data from the first detected BNS event GW170817, by postprocessing the publicly available posteriors of the LIGO-Virgo Collaboration released with Refs. [4,10]. In all of the analysis setups, the NS spins are aligned with the orbital angular momentum and the spin magnitudes are restricted to the "low-spin" prior range $\chi_{A,B} \in [-0.05, 0.05]$.

A. Results

For the threshold-mass method (Sec. III A), we process the posteriors of the spectral parameters $(\gamma_0, \gamma_1, \gamma_2, \gamma_3)$ published in Ref. [10]

 (i) without imposing an implicit constraint on $M_{\text{TOV}}^{\text{max}}$;
 (ii) with the additional hard cut of $M_{\text{TOV}}^{\text{max}} \geq 1.97\ M_{\odot}$, corresponding to a 1σ conservative estimate of the PSR J0348+0432 mass measurement $2.01 \pm 0.04\ M_{\odot}$ [47];
 (iii) with the additional probabilistic weight quantifying the probability of $M_{\text{TOV}}^{\text{max}}$ being heavier than the PSR J0348+0432 mass.

For the threshold-$\tilde{\Lambda}$ method, we process published posteriors on tidal parameters from a number of different analyses. In particular, we consider methods that extend the

binary black hole parameter space by the matter-related parameters

 (i) $(\tilde{\Lambda}, \delta\tilde{\Lambda})$, using four different waveform models (IMRPhenomPv2NRtidal, IMRPhenomDNR-tidal, SEOBNRT, TaylorF2);
 (ii) $\Lambda_s = (\Lambda_A + \Lambda_B)/2$, the symmetric tidal parameter, using IMRPhenomPv2NRtidal, along with the use of the EOS-insensitive relation for the antisymmetric tidal parameter $\Lambda_a(\Lambda_s, q)$ (see [10]), which can then be mapped to $\tilde{\Lambda}$;
 (iii) $\vec{\gamma} = (\gamma_0, \gamma_1, \gamma_2, \gamma_3)$ parametrizing the EOS, from which $\tilde{\Lambda}$ can be derived, with and without a constraint on $M_{\text{TOV}}^{\text{max}}$ (see parametrized EOS method of [10]).

First, for the threshold-mass method we show in Fig. 4 the joint posterior of total mass M and the threshold mass M_{thr} (left) as well as the cumulative distribution function of their ratio M/M_{thr} (right), obtained with the threshold-mass analysis with and without the constraint $M_{\text{TOV}}^{\text{max}} \geq 1.97\ M_{\odot}$. The latter plot should be interpreted as the probability of prompt collapse as a function of k_{thr}, if we pretended to be totally agnostic on k_{thr}. Without the maximum mass constraint, the collapse probability ranges from $P_{\text{PC}} \sim 0.2$ to $P_{\text{PC}} \sim 0.85$ for the expected range of k_{thr} (see orange line and white region in the plot). Including the constraint $M_{\text{TOV}}^{\text{max}} \geq 1.97\ M_{\odot}$ strongly disfavors a prompt collapse: $P_{\text{PC}} = 0$ if $k_{\text{thr}} > 1.4$, growing up to $P_{\text{PC}} \sim 0.5$ if $k_{\text{thr}} \sim 1.3$, if for very soft EOS and NS compactness $C_{\text{max}} \sim 0.33$.

However, k_{thr} is not an independent unknown parameter; using the results of Sec. II A we estimate the value of k_{thr} and M_{thr} from the EOS parameters $\vec{\gamma}$. The resulting posterior of M/M_{thr} is plotted as a cumulative distribution in Fig. 5. Here too, we find a significant difference between the analyses with and without the $M_{\text{TOV}}^{\text{max}}$ constraint, that estimate the prompt-collapse probability at 0.09 and 0.59, respectively. The reason is that the $M_{\text{TOV}}^{\text{max}}$ constraint
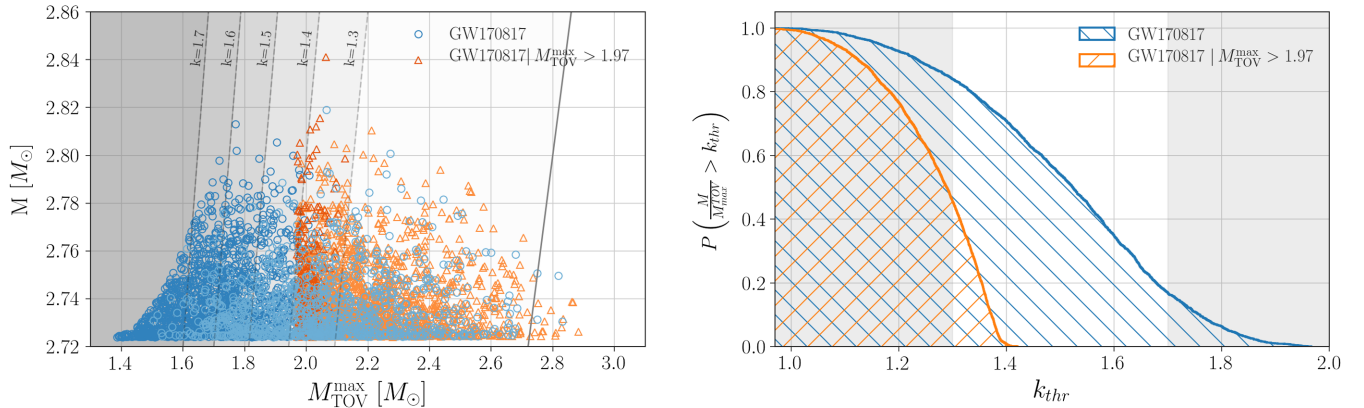

FIG. 4.   Prompt-collapse analysis of GW170817 based on threshold tidal parameter method, with and without a hard $M_{\text{TOV}}^{\text{max}}$ constraint at 1.97 $M_{\odot}$. Left: Joint posteriors in the M-$M_{\text{TOV}}^{\text{max}}$ plane when analyzing with (orange) and without (blue) a prior cut on $M_{\text{TOV}}^{\text{max}}$. Dark (light) colored points lie above (below) the mass threshold of prompt collapse. Contours of k_{thr} within the typical range [1.3, 1.7] are shown as gray shaded regions. Right: Probability of prompt collapse as a function of k_{thr} with and without the $M_{\text{TOV}}^{\text{max}}$ constraint [before making use of Eq. (3)].
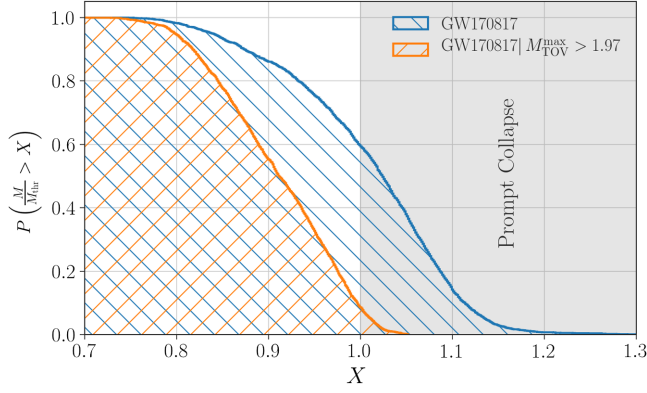
FIG. 5.   Cumulative posterior distribution on the ratio M/M_{thr}. The fraction of the posterior that lies above unity gives the probability of prompt collapse with (blue) and without (orange) a constraint of $M_{\text{TOV}}^{\text{max}} \geq 1.97\,\text{M}_\odot$.
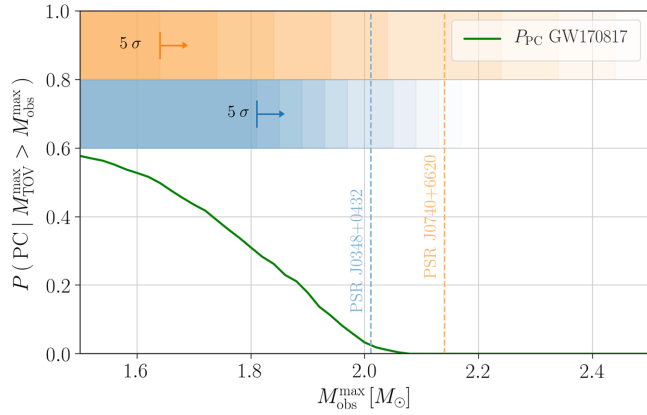

FIG. 6.   The probability of prompt collapse for GW170817 as a function of the heaviest observed NS mass. The Gaussian mass measurements of PSR J0348+0432 and PSR J0740+6620 are represented in the shaded exclusion regions at different confidence levels, up to 5σ.

removes part of the EOS parameter space that is too soft to support a NS mass of $1.97\,\text{M}_\odot$ (and will most likely predict a prompt collapse). The effect on P_{PC} is significant, since the recovered binary parameters of GW170817 happen to
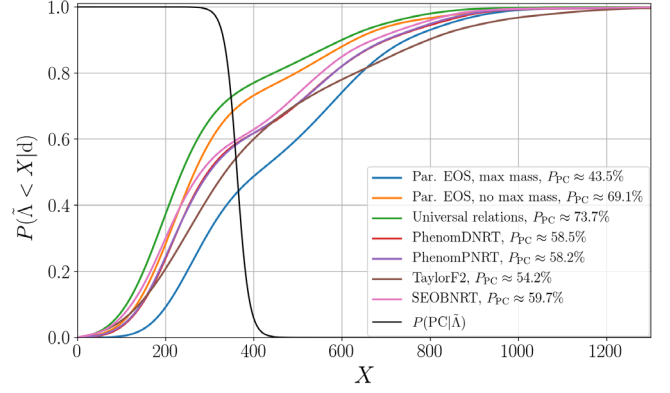

FIG. 7.   Probability of prompt collapse for GW170817 based on the threshold-$\tilde\Lambda$ method for different analysis setups. Colored curves plot the cumulative posterior probability distribution for $\tilde\Lambda$. The solid black sigmoid curve gives the prior probability of prompt collapse at each value of $\tilde\Lambda$, based on NR simulations. The prompt-collapse probability can be visually estimated by the value of each curve as it crosses the transition region.

lie close to the prompt-collapse threshold. We now estimate P_{PC} as a function of the maximum-mass constraint, by varying the lower bound on $M_{\text{TOV}}^{\text{max}}$ that we impose on the posterior samples. The results are shown in Fig. 6 where, as expected, we observe the prompt-collapse probability to be decreasing as we increase the lower bound on $M_{\text{TOV}}^{\text{max}}$ (therefore requiring the EOS to be stiff enough to support higher masses and effectively pushing the threshold mass to larger values). To put these values into context, the mass measurements of the two heaviest pulsars observed to date, namely PSR J0348+0432 [47] and PSR J0740+6620 [48], give the exclusion regions for $M_{\text{TOV}}^{\text{max}}$ that are shown in the shaded bands at different confidence levels up to 5σ.

Figure 7 shows the prompt-collapse probability obtained with the threshold-$\tilde\Lambda$ method (cf. Fig. 3, left panel) We find a prompt-collapse probability between $P_{\text{PC}} \sim 43\%$ and 74%, depending on the waveform approximant used for the analysis and on the inference method employed. The data from the EOS inference employed also in the threshold-mass analysis give the smallest prompt-collapse

TABLE II.   Summary of GW170817 results derived with the threshold-mass and the threshold-$\tilde\Lambda$ methods: probability of prompt collapse for different sets of analyses published by the LVC.

Method	Inferred parameters	Approximant	Ref.	P_{PC}
M_{thr}	$\vec\gamma$	`IMRPhenomPv2NRtidal`	[10]	0.59
M_{thr}	$\vec\gamma \| M_{\text{TOV}}^{\text{max}} \geq 1.97\,\text{M}_\odot$	`IMRPhenomPv2NRtidal`	[10]	0.09
$\tilde\Lambda_{\text{thr}}$	$\vec\gamma$	`IMRPhenomPv2NRtidal`	[10]	0.69
$\tilde\Lambda_{\text{thr}}$	$\vec\gamma \| M_{\text{TOV}}^{\text{max}} \geq 1.97\,\text{M}_\odot$	`IMRPhenomPv2NRtidal`	[10]	0.44
$\tilde\Lambda_{\text{thr}}$	$\tilde\Lambda$	`TaylorF2`	[4]	0.54
$\tilde\Lambda_{\text{thr}}$	$\tilde\Lambda$	`IMRPhenomPv2NRtidal`	[4]	0.58
$\tilde\Lambda_{\text{thr}}$	$\tilde\Lambda$	`IMRPhenomDNRtidal`	[4]	0.59
$\tilde\Lambda_{\text{thr}}$	$\tilde\Lambda$	`SEOBNRT`	[4]	0.60
$\tilde\Lambda_{\text{thr}}$	Λ_s	`IMRPhenomPv2NRtidal`	[10]	0.74

probability as a result of imposing the maximum mass constraint. If the constraint is relaxed, the probability grows to 69%. All the analysis performing inference on $\tilde{\Lambda}$ give prompt-collapse probability between 54% and 60%; the waveform approximants estimating the largest $\tilde{\Lambda}$ clearly give the smaller probabilities. The largest prompt-collapse probability is obtained using the EOS-insensitive relations in the Λ_s inference and employing the $\tilde{\Lambda}$ threshold. This can be understood as the combined effect of using `IMRPhenomPv2NRtidal` as a template waveform model, which tends to introduce a systematic bias favoring prompt collapse (see discussion in Appendix B) and not having a constraint on $M_{\text{TOV}}^{\max}$.

Resulting values for the probability of prompt collapse P_{PC} from the above analyses are listed in Table II. We observe that the parameters of GW170817 are measured around the threshold region both for the threshold-mass method and for the threshold-$\tilde{\Lambda}$ method. Thus, overall there seems to be no definite answer as to whether the BNS merger was followed by a prompt collapse to a BH. However, if we focus on the analyses where the $M_{\text{TOV}}^{\max}$ constraint can be imposed, to account for the mass measurement of PSR J0348+0432, we see that the prompt-collapse hypothesis is strongly disfavored.

We also point out that the GW170817 inference of tidal effects using various point-mass waveform approximants combined with NRTidal gives posteriors with a bimodal distribution peaked around $\tilde{\Lambda} \sim 200$ and $\tilde{\Lambda} \sim 600$ and support up to $\tilde{\Lambda} \sim 800$; while using `TaylorF2` and EOB approximants it gives a single broader peak at $\tilde{\Lambda} \sim 300$ [4,5]. Independent analysis confirm these findings [74–76].

VI. CONCLUSION

We proposed two methods to infer prompt black-hole formation from the analysis of the inspiral gravitational wave of a binary neutron merger. Both methods rely on numerical-relativity models of the prompt collapse threshold for a quasicircular and nonspinning binary neutron star merger. The methods are validated with a set of 17 injection and recovery experiments and verified against data from numerical-relativity simulations. All the signals were correctly recovered with the exception of a few cases close or at the collapse threshold. Improving such cases will require more precise numerical-relativity models and simulations. We conclude that our analysis could be robustly applied to GW170817-like signals (single events) captured by Advanced LIGO-Virgo at designed sensitivity. We also point out that waveform systematics may introduce important biases in the near-threshold region.

Application of these two methods on the GW170817 data gives no definitive answer to whether the BNS merger was followed by a prompt collapse into a BH, as the recovered masses and tidal parameters of the binary appear to lie in the vicinity of the threshold. However, if a constraint is applied on the maximum irrotational NS mass supported by the EOS, that is compatible with the mass measurements of PSR J0348+0432 and PSR J0740+6620, then we observe a strong preference against the prompt-collapse hypothesis. Finally, we note that the universal character of the threshold mass, as a parameter that is common across all NSs that share the same EOS, allows for its measurement to be seamlessly updated with information from GW and EM observations alike.

APPENDIX A: PROMPT-COLLAPSE THRESHOLD FROM NR DATA

We collect NR data for the prompt-collapse threshold k_{thr} from Refs. [27,28,31,34] into Table III.

In the first three references, the collapse threshold is estimated by performing simulations with a given EOS and different masses and then linearly interpolating between the two simulations that bracket the threshold. The uncertainty on the k_{thr} is thus determined not only by the grid resolution of the simulations but also by how close the two simulations bracket the threshold. Typical relative errors are at the level of 5% although, surprisingly, detailed grid resolution studies for this application are missing. In Ref. [31] the collapse threshold for a specific EOS is determined as the binary mass for which the merger remnant collapses over the free-fall timescale of a $M_{\text{TOV}}^{\max}$ NS. The actual value of M_{thr} is computed using an extrapolation of an exponential fit of the results obtained by a few prompt-collapse simulations. The reported error is also the one obtained by the exponential fit. Despite

TABLE III. Numerical-relativity data used for determining the prompt-collapse mass threshold coefficient $k_{\rm thr}$.

EOS	$C_{\rm max}$	$k_{\rm thr}$	$\delta k_{\rm thr}$	$M_{\rm TOV}^{\rm max}$ [M$_\odot$]	$M_{\rm thr}$ [M$_\odot$]	Ref.
APR4	0.329	1.243	0.023	2.21	2.80	[27]
SLy	0.307	1.342	0.024	2.06	2.76	[27]
H3	0.224	1.566	0.056	1.79	2.90	[27]
H4	0.258	1.452	0.025	2.03	2.95	[27]
ALF2	0.260	1.414	0.024	1.99	2.81	[27]
NL3	0.307	1.380	0.018	2.79	3.85	[28]
GS1	0.306	1.400	0.018	2.75	3.85	[28]
LS375	0.325	1.347	0.018	2.71	3.65	[28]
DD2	0.300	1.384	0.021	2.42	3.35	[28]
Shen	0.250	1.554	0.023	2.22	3.45	[28]
TM1	0.260	1.561	0.023	2.21	3.45	[28]
SFHx	0.292	1.432	0.023	2.13	3.05	[28]
GS2	0.262	1.555	0.024	2.09	3.25	[28]
SFHo	0.294	1.432	0.024	2.06	2.95	[28]
LS220	0.284	1.495	0.025	2.04	3.05	[28]
TMA	0.247	1.609	0.025	2.02	3.25	[28]
IUF	0.255	1.564	0.026	1.95	3.05	[28]
LS220	0.284	1.445	0.024	2.04	2.95	[34]
BHBΛϕ	0.268	1.469	0.047	2.11	3.10	[34]
ALF2	0.260	1.444	0.063	1.99	2.86	[34]
H4	0.258	1.529	0.049	2.03	3.10	[34]
SLy	0.307	1.395	0.061	2.06	2.86	[34]
BHBΛϕ	0.268	1.503	0.024	2.11	3.17	[31]
DD2	0.300	1.364	0.021	2.42	3.30	[31]
SFHo	0.294	1.391	0.024	2.06	2.87	[31]
TM1	0.260	1.520	0.023	2.21	3.36	[31]

FIG. 8. Numerical-relativity fits of the prompt-collapse threshold $k_{\rm thr}$. Top: $k_{\rm thr}$ as a function of the maximum compactness $C_{\rm max}$; see Table III. The black line represents the fit of the results reported in [28,31,34]. Bottom: Coefficients of the linear fits (with errors) obtained by the single datasets and by the dataset used to produce the fit used in this work.

providing consistent results, the error estimate is qualitatively different from the other approaches and counterintuitively the fewer the simulations, the smaller the uncertainties. We thus select the $M_{\rm thr}$ for which at least three simulations were performed and we assign to all of them the relative error obtained by their DD2 model, since this is the model with more points. We stress that this relative error is comparable to the smallest relative errors used in the other works.

The data are plotted as a function of the maximum compactness and shown in the top panel of Fig. 8. All the data show an approximate linear correlation with $C_{\rm max}$ although part of the data of Ref. [27] appear to systematically underestimate the threshold with respect to the other datasets. We perform several linear fits combining the datasets and propagating the uncertainties. The fit coefficients and their errors are reported in the bottom panel of Fig. 8. The different sets of coefficients are essentially compatible with each other, and the errors become smaller when more points are included. The equation we use in the main body [Eq. (3)] is the best fit given by the combination of the data of Refs. [28,31,34].
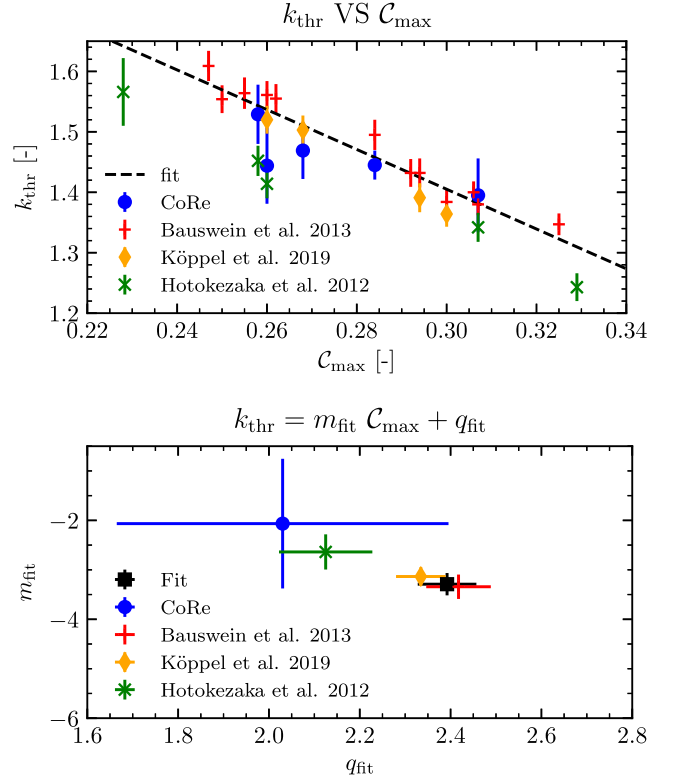
APPENDIX B: WAVEFORM SYSTEMATICS

Our injection experiments highlight systematics biases in the recovery of the TEOBResumS waveforms when using the IMRPhenomPv2NRtidal as our template model, while results are overall consistent when TaylorF2 is employed with or without a high cutoff frequency of 1024 Hz. Representative measurements of the tidal parameter $\tilde{\Lambda}$ are shown in Fig. 9 for two injections with different EOS. A similar bias between TEOBResumS and IMRPhenomPv2NRtidal is visible in the injections of Refs. [72,73] performed at SNR 100, but so far this has not been systematically investigated nor explained. We plan to do so in a forthcoming publication. Here, we use the IMRPhenomPv2NRtidal results to discuss how waveform systematics can affect the prompt-collapse inference with our two methods. In the comparison plots of Fig. 9 we show how analyzing the same signal with different waveform models can affect the estimated prompt-collapse probability; in particular IMRPhenomPv2NRtidal tends to underestimate tidal deformabilities and therefore overestimate $P_{\rm PC}$. A similar effect is observed in the threshold-mass results for the same injections in the left panel of Fig. 10, where $M/M_{\rm thr}$ is overestimated
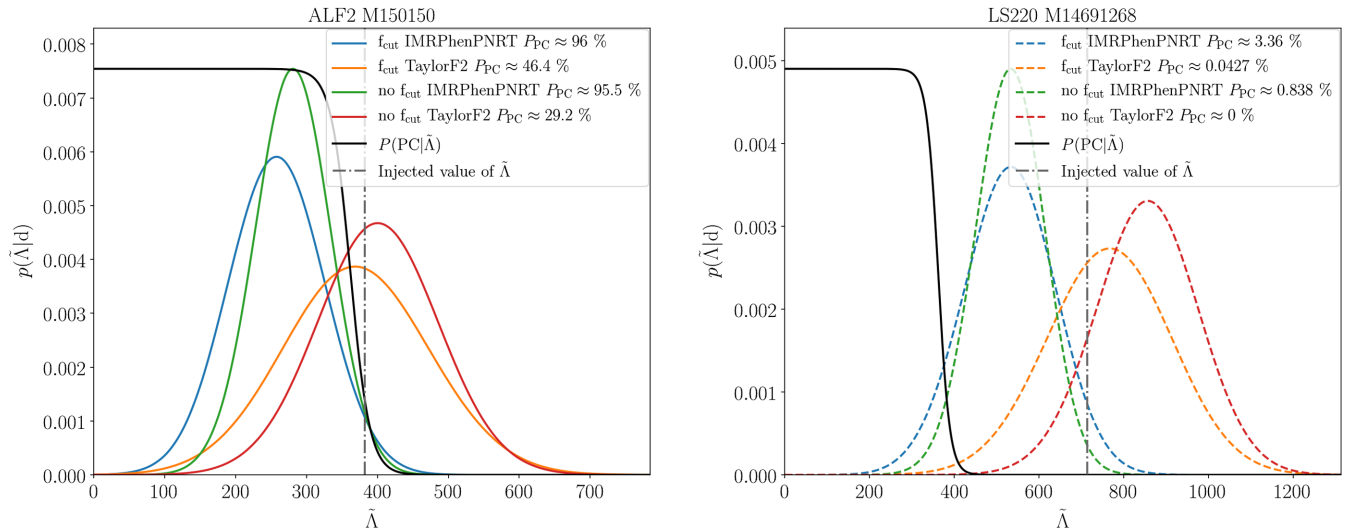
FIG. 9.　Recovery of TEOBResumS $\tilde{\Lambda}$ with TaylorF2 and IMRPhenomPv2NRtidal and two maximal cutoff frequencies 1024 and 2048 Hz for representative injections. In our experiments IMRPhenomPv2NRtidal systematically underestimates the injected TEOBResumS $\tilde{\Lambda}$, while TaylorF2 with cutoff frequency 1024 Hz give the most consistent results.
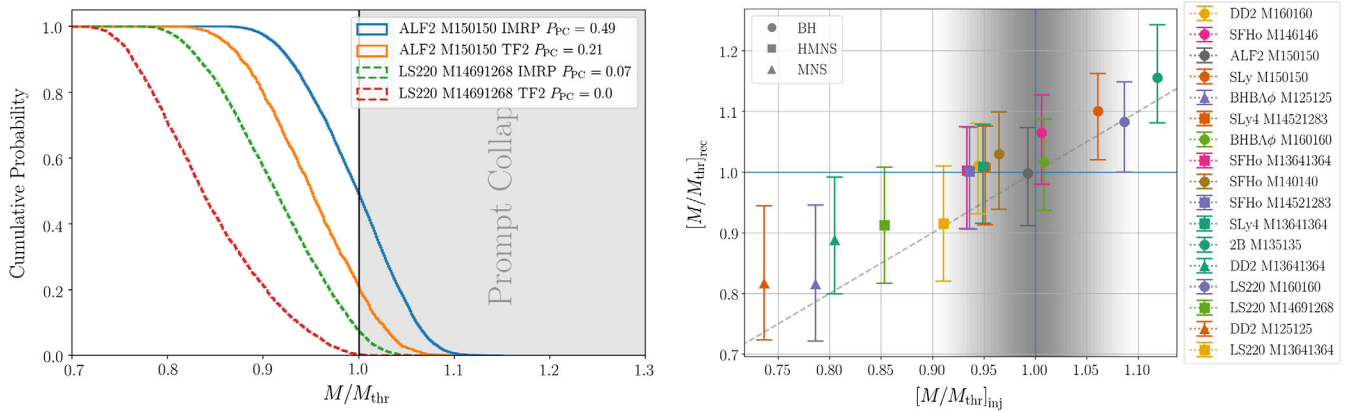

FIG. 10.　Left: Recovery of TEOBResumS mass relative to threshold mass with TaylorF2 and IMRPhenomPv2NRtidal for the two runs shown in Fig. 9. Waveform systematics may induce significant effects on the threshold-mass parameter analysis. Right: Summary of threshold-mass analysis on the simulated signals of Table I using IMRPhenomPv2NRtidal.
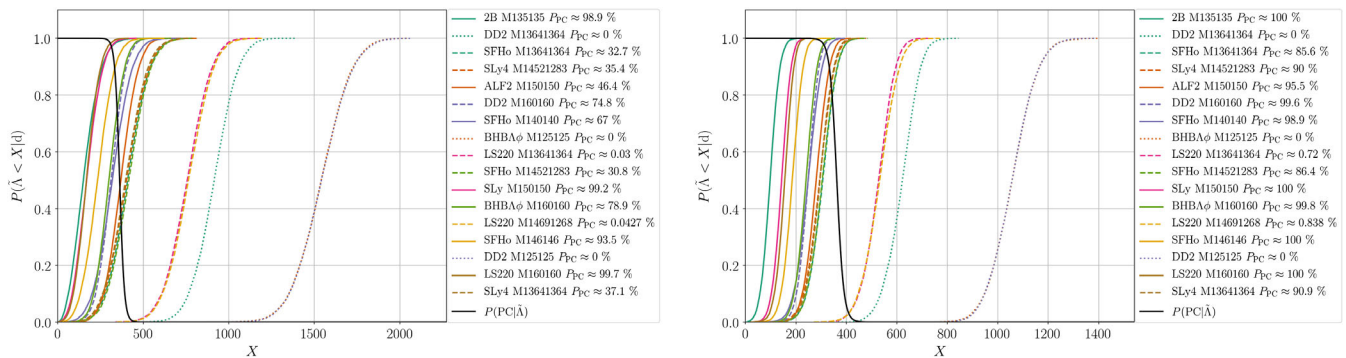

FIG. 11.　Waveform systematics effects on the threshold tidal parameter analysis. Recovering with TaylorF2 and cutoff 1024 Hz (left) gives consistent results with the injection except for binaries with $\Lambda \sim \tilde{\Lambda}_{\mathrm{thr}}$ for which a 50–50 chance of prompt is returned. Recovering with IMRPhenomPv2NRtidal and cutoff 2048 Hz (right) gives consistent results with the injection except for binaries with $\Lambda \sim \tilde{\Lambda}_{\mathrm{thr}}$ for it incorrectly favors prompt collapse.

by `IMRPhenomPv2NRtidal` (and thus so is P_{PC}). Overall, we find the significance of waveform systematics to be limited to the cases close to the collapse threshold.

Figure 11 summarizes waveform systematics effects on the threshold tidal parameter analysis. We find that the prompt-collapse inference with `TaylorF2` and cutoff 1024 Hz gives consistent results with the injection except for binaries with $\Lambda \sim \tilde{\Lambda}_{\text{thr}}$. For the DD2 $1.59 + 1.59$ BNS ($\tilde{\Lambda} = 332$) and the two SLy binaries ($\tilde{\Lambda} \sim 401$) the method estimates, respectively, a 75% and $\sim$40% probability of prompt collapse while the merger result in a HMNS. In the former case the binary is at the collapse threshold and the HMNS is very short lived (3 ms). Hence it could be simply a result of our uncertainties. In the latter case the binaries are slightly above the collapse threshold and the prediction appears to have a genuine systematic error of the method. Similarly, for SFHo $1.40 + 1.40$ ($\tilde{\Lambda} = 334$) and ALF2 $1.50 + 1.50$ ($\tilde{\Lambda} = 382$) the method predicts 33% and 54% probability, respectively, of producing a NS remnant while the simulations indicate prompt BH formation.

Recovering with `IMRPhenomPv2NRtidal` systematically underestimates the injected `TEOBResumS` $\tilde{\Lambda}$, the effect being worst for cutoff frequency 1024 Hz and minimized by cutoff 2048 Hz. The result can be in part understood from the fact that the low-frequency limit of the `NRtidal` is accurate only to the leading-order post-Newtonian tidal term [71,77]. The same systematic trend can be seen in the threshold-mass analysis summarized in the right panel of Fig. 10, which is more pronounced in the less compact binaries. The errors in the prompt-collapse analysis due to the numerical fits on k_{thr} discussed above are now combined with those from the waveform systematics. As a result, the method predicts correctly the prompt collapse of ALF2 $1.59 + 1.59$ and SFHo $1.40 + 1.40$ (thanks to a "cancellation" of systematic errors) but incorrectly favors prompt collapse for the SLy binaries.

APPENDIX C: EFFECT OF $M_{\text{TOV}}^{\max}$ CONSTRAINT

In the threshold-mass method, sampling the EOS parameter space directly allowed us to impose conditions on the maximum stable nonrotating NS mass $M_{\text{TOV}}^{\max}$. In this section we examine the effect that different choices of this constraint may have on estimating the probability of prompt collapse.

First we review the results of the injection study of Sec. IV when imposing a $M_{\text{TOV}}^{\max}$ constraint based on the mass measurement of PSR J0348+0432. Results are summarized in Fig. 12. When comparing against Fig. 2, we observe a systematic trend to lower values of recovered M/M_{thr}. This can be interpreted as a push toward higher values of M_{thr}, which is expected, since a soft part of the space of EOS is effectively removed from our prior. Note
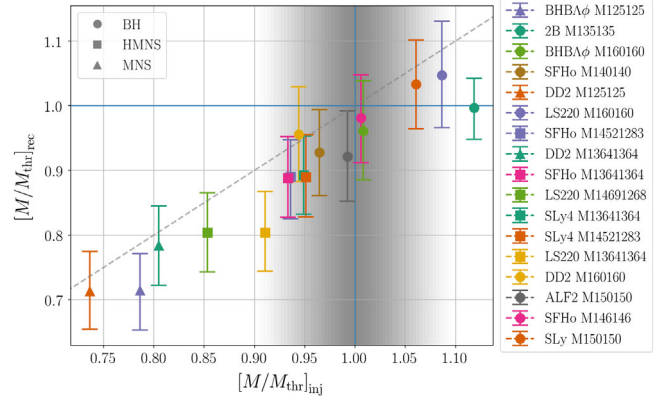

FIG. 12. Effect of $M_{\text{TOV}}^{\max}$ constraint on the threshold-mass parameter analysis (see Fig. 2) using the PSR J0348+0432 mass measurement.

the peculiar behavior of the 2B BNS as a consequence of the fact that the maximum mass for that EOS violates the prior imposed in the analysis.

We now move on to the analysis of GW170817 data using the spectral EOS parametrization and consider the following choices:

   (i) no constraint on $M_{\text{TOV}}^{\max}$;

  (ii) a hard constraint of $M_{\text{TOV}}^{\max} \geq 1.97 \, M_{\odot}$, corresponding to a conservative 1σ bound on the mass of PSR J0348+0432;

 (iii) a probabilistic constraint based on the mass measurement of PSR J0348+0432, which follows the Gaussian PDF $\mathcal{N}(2.01, 0.04)$;

 (iv) a probabilistic constraint based on the recent observation of PSR J0740+6620, which follows the Gaussian PDF $\mathcal{N}(2.14, 0.10)$.

The results are illustrated in Fig. 13. We find that if the heavy-NS measurements are taken into account, the prompt-collapse probability tends to zero (even more so than in the case of a hard cut at $1.97 \, M_{\odot}$).
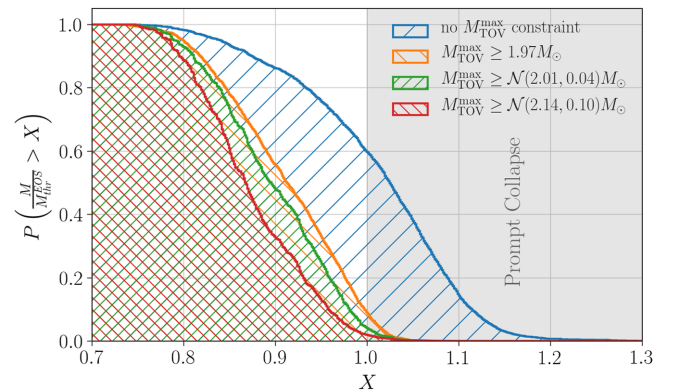

FIG. 13. Cumulative distribution of the total mass M divided by the threshold mass M_{thr} for different choices of the $M_{\text{TOV}}^{\max}$ constraint. The value at $X = 1$ gives the probability of prompt collapse.
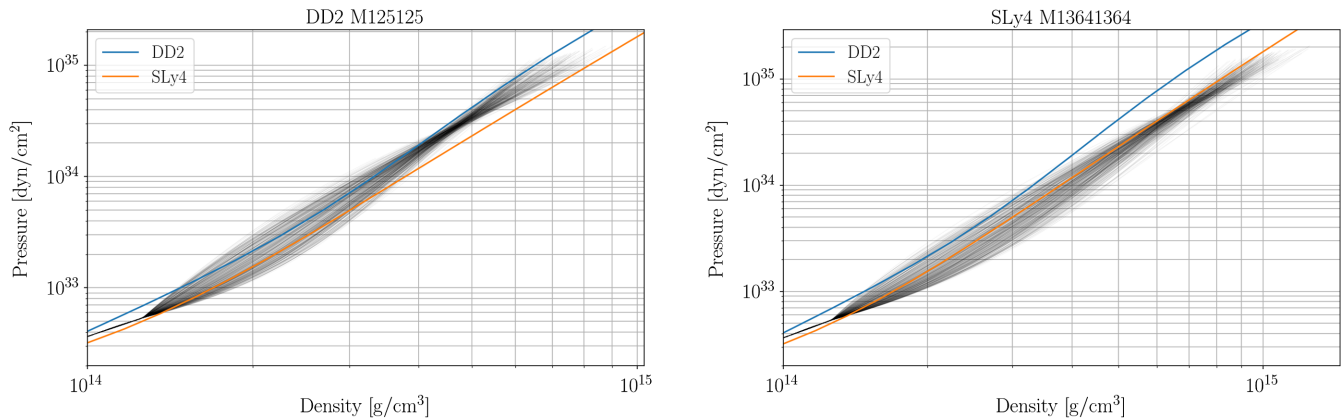
FIG. 14. Reconstruction of $P(\rho)$ for the underlying EOS models DD2 (left) and SLy4 (right), from the posterior PDF on the spectral parameters $\vec{\gamma}$. The posteriors in the two cases converge towards the correct EOS curve, with a "focal point" around $2\rho_{nuc}$. The curves end at the central density of their corresponding heaviest stable NS.

APPENDIX D: EOS RECONSTRUCTION

In our threshold-mass method we have employed the spectral family of Ref. [44] to parametrize the EOS. It is instructive to examine whether the posterior PDF on the EOS parameters $\vec{\gamma}$ faithfully reconstructs the injected model, within the margins of our measurement error. Two typical cases are illustrated in Fig. 14, where the

reconstructed $P(\rho)$ curves are clearly distinguishable from each other and faithfully follow the corresponding underlying model. In particular we observe the separation becoming more clear around a "focal point" at $\sim 2\rho_{nuc}$, which happens to be close to the typical central density of the NS, which largely determines the bulk properties of the star.

[1] J. Aasi *et al.* (LIGO Scientific Collaboration), Classical Quantum Gravity **32**, 074001 (2015).

[2] F. Acernese *et al.* (Virgo Collaboration), Classical Quantum Gravity **32**, 024001 (2015).

[3] B. P. Abbott *et al.* (Virgo and LIGO Scientific Collaborations), Phys. Rev. Lett. **119**, 161101 (2017).

[4] B. P. Abbott *et al.* (LIGO Scientific and Virgo Collaborations), Phys. Rev. X **9**, 011001 (2019).

[5] B. P. Abbott *et al.* (LIGO Scientific and Virgo Collaborations), Phys. Rev. X **9**, 031040 (2019).

[6] T. Damour, A. Nagar, and L. Villain, Phys. Rev. D **85**, 123007 (2012).

[7] M. Favata, Phys. Rev. Lett. **112**, 101101 (2014).

[8] W. Del Pozzo, T. G. F. Li, M. Agathos, C. Van Den Broeck, and S. Vitale, Phys. Rev. Lett. **111**, 071101 (2013).

[9] B. D. Lackey and L. Wade, Phys. Rev. D **91**, 043002 (2015).

[10] B. P. Abbott *et al.* (LIGO Scientific and Virgo Collaborations), Phys. Rev. Lett. **121**, 161101 (2018).

[11] B. P. Abbott *et al.* (LIGO Scientific and Virgo Collaborations), Astrophys. J. **875**, 160 (2019).

[12] B. P. Abbott *et al.* (Virgo, Fermi-GBM, INTEGRAL, ad LIGO Scientific Collaborations), Astrophys. J. **848**, L13 (2017).

[13] E. Troja *et al.*, Nature (London) **551**, 71 (2017).

[14] B. P. Abbott *et al.* (GROND, SALT Group, OzGrav, DFN, INTEGRAL, Virgo, Insight-Hxmt, MAXI Team, Fermi-LAT, J-GEM, RATIR, IceCube, CAASTRO, LWA, ePESSTO, GRAWITA, RIMAS, SKA South Africa/MeerKAT, H.E.S.S., 1M2H Team, IKI-GW Follow-up, Fermi GBM, Pi of Sky, DWF (Deeper Wider Faster Program), Dark Energy Survey, MASTER, AstroSat Cadmium Zinc Telluride Imager Team, Swift, Pierre Auger, ASKAP, VINROUGE, JAGWAR, Chandra Team at McGill University, TTU-NRAO, GROWTH, AGILE Team, MWA, ATCA, AST3, TOROS, Pan-STARRS, NuSTAR, ATLAS Telescopes, BOOTES, CaltechNRAO, LIGO Scientific, High Time Resolution Universe Survey, Nordic Optical Telescope, Las Cumbres Observatory Group, TZAC Consortium, LOFAR, IPN, DLT40, Texas Tech University, HAWC, ANTARES, KU, Dark Energy Camera GW-EM, CALET, Euro VLBI Team, and ALMA Collaborations), Astrophys. J. **848**, L12 (2017).

[15] D. A. Coulter *et al.*, Science **358**, 1556 (2017).

[16] R. Chornock *et al.*, Astrophys. J. **848**, L19 (2017).

[17] M. Nicholl *et al.*, Astrophys. J. **848**, L18 (2017).

[18] P. S. Cowperthwaite *et al.*, Astrophys. J. **848**, L17 (2017).

[19] N. R. Tanvir *et al.*, Astrophys. J. **848**, L27 (2017).

[20] M. Tanaka *et al.*, Publ. Astron. Soc. Jpn. **69**, 102 (2017).

[21] B. Margalit and B. D. Metzger, Astrophys. J. **850**, L19 (2017).

[22] M. Shibata, S. Fujibayashi, K. Hotokezaka, K. Kiuchi, K. Kyutoku, Y. Sekiguchi, and M. Tanaka, Phys. Rev. D **96**, 123012 (2017).

[23] M. Shibata and K. Uryu, Phys. Rev. D **61**, 064001 (2000).

[24] M. Shibata, K. Taniguchi, and K. Uryu, Phys. Rev. D **68**, 084020 (2003).

[25] M. Anderson, E. W. Hirschmann, L. Lehner, S. L. Liebling, P. M. Motl, D. Neilsen, C. Palenzuela, and J. E. Tohline, Phys. Rev. D **77**, 024006 (2008).

[26] M. Thierfelder, S. Bernuzzi, and B. Brügmann, Phys. Rev. D **84**, 044012 (2011).

[27] K. Hotokezaka, K. Kyutoku, H. Okawa, M. Shibata, and K. Kiuchi, Phys. Rev. D **83**, 124008 (2011).

[28] A. Bauswein, T. Baumgarte, and H. T. Janka, Phys. Rev. Lett. **111**, 131101 (2013).

[29] L. Rezzolla, E. R. Most, and L. R. Weih, Astrophys. J. **852**, L25 (2018).

[30] D. Radice, A. Perego, S. Bernuzzi, and B. Zhang, Mon. Not. R. Astron. Soc. **481**, 3670 (2018).

[31] S. Kppel, L. Bovard, and L. Rezzolla, Astrophys. J. **872**, L16 (2019).

[32] A. Bauswein, O. Just, H.-T. Janka, and N. Stergioulas, Astrophys. J. **850**, L34 (2017).

[33] M. Ruiz, S. L. Shapiro, and A. Tsokaros, Phys. Rev. D **97**, 021501 (2018).

[34] F. Zappa, S. Bernuzzi, D. Radice, A. Perego, and T. Dietrich, Phys. Rev. Lett. **120**, 111101 (2018).

[35] T. Dietrich, D. Radice, S. Bernuzzi, F. Zappa, A. Perego, B. Brgmann, S. V. Chaurasia, R. Dudi, W. Tichy, and M. Ujevic, Classical Quantum Gravity **35**, 24LT01 (2018).

[36] T. Hinderer, Astrophys. J. **677**, 1216 (2008).

[37] T. Damour and A. Nagar, Phys. Rev. D **80**, 084035 (2009).

[38] T. Binnington and E. Poisson, Phys. Rev. D **80**, 084018 (2009).

[39] T. Damour and O. M. Lecian, Phys. Rev. D **80**, 044017 (2009).

[40] T. Damour and A. Nagar, Phys. Rev. D **81**, 084016 (2010).

[41] N. Grlebeck, Phys. Rev. Lett. **114**, 151102 (2015).

[42] S. Bernuzzi, A. Nagar, S. Balmelli, T. Dietrich, and M. Ujevic, Phys. Rev. Lett. **112**, 201101 (2014).

[43] J. Veitch *et al.*, Phys. Rev. D **91**, 042003 (2015).

[44] L. Lindblom, Phys. Rev. D **82**, 103011 (2010).

[45] M. F. Carney, L. E. Wade, and B. S. Irwin, Phys. Rev. D **98**, 063004 (2018).

[46] J. S. Read, B. D. Lackey, B. J. Owen, and J. L. Friedman, Phys. Rev. D **79**, 124032 (2009).

[47] J. Antoniadis, P. C. Freire, N. Wex, T. M. Tauris, R. S. Lynch *et al.*, Science **340**, 1233232 (2013).

[48] H. T. Cromartie *et al.*, Nat. Astron., https://doi.org/10.1038/s41550-019-0880-2.

[49] K. Kiuchi, K. Kyutoku, M. Shibata, and K. Taniguchi, Astrophys. J. **876**, L31 (2019).

[50] D. Radice, A. Perego, K. Hotokezaka, S. A. Fromm, S. Bernuzzi, and L. F. Roberts, Astrophys. J. **869**, 130 (2018).

[51] S. Bernuzzi, A. Nagar, T. Dietrich, and T. Damour, Phys. Rev. Lett. **114**, 161103 (2015).

[52] D. Radice, A. Perego, F. Zappa, and S. Bernuzzi, Astrophys. J. **852**, L29 (2018).

[53] D. Radice, S. Bernuzzi, W. Del Pozzo, L. F. Roberts, and C. D. Ott, Astrophys. J. **842**, L10 (2017).

[54] A. Perego, S. Bernuzzi, and D. Radice, Eur. Phys. J. A **55**, 124 (2019).

[55] D. Radice and L. Rezzolla, Astron. Astrophys. **547**, A26 (2012).

[56] D. Radice, L. Rezzolla, and F. Galeazzi, Mon. Not. R. Astron. Soc. **437**, L46 (2014).

[57] D. Radice, L. Rezzolla, and F. Galeazzi, Classical Quantum Gravity **31**, 075012 (2014).

[58] S. Banik, M. Hempel, and D. Bandyopadhyay, Astrophys. J. Suppl. Ser. **214**, 22 (2014).

[59] S. Typel, G. Ropke, T. Klahn, D. Blaschke, and H. H. Wolter, Phys. Rev. C **81**, 015803 (2010).

[60] M. Hempel and J. Schaffner-Bielich, Nucl. Phys. **A837**, 210 (2010).

[61] J. M. Lattimer and F. D. Swesty, Nucl. Phys. **A535**, 331 (1991).

[62] A. W. Steiner, M. Hempel, and T. Fischer, Astrophys. J. **774**, 17 (2013).

[63] A. S. Schneider, L. F. Roberts, and C. D. Ott, Phys. Rev. C **96**, 065802 (2017).

[64] T. W. Baumgarte, S. L. Shapiro, and M. Shibata, Astrophys. J. **528**, L29 (2000).

[65] G. B. Cook, S. L. Shapiro, and S. A. Teukolsky, Astrophys. J. **424**, 823 (1994).

[66] A. Nagar *et al.*, Phys. Rev. D **98**, 104052 (2018).

[67] S. Akcay, S. Bernuzzi, F. Messina, A. Nagar, N. Ortiz, and P. Rettegno, Phys. Rev. D **99**, 044051 (2019).

[68] A. Nagar and P. Rettegno, Phys. Rev. D **99**, 021501 (2019).

[69] https://bitbucket.org/eob_ihes/teobresums/src/master/, TEOBResums code.

[70] LIGO Scientific Collaboration, LIGO Algorithm Library—LALSuite, free software (GPL) (2018).

[71] T. Dietrich, S. Bernuzzi, and W. Tichy, Phys. Rev. D **96**, 121501 (2017).

[72] R. Dudi, F. Pannarale, T. Dietrich, M. Hannam, S. Bernuzzi, F. Ohme, and B. Bruegmann, Phys. Rev. D **98**, 084061 (2018).

[73] F. Messina, R. Dudi, A. Nagar, and S. Bernuzzi, Phys. Rev. D **99**, 124051 (2019).

[74] S. De, D. Finstad, J. M. Lattimer, D. A. Brown, E. Berger, and C. M. Biwer, Phys. Rev. Lett. **121**, 091102 (2018); **121**, 259902(E) (2018).

[75] L. Dai, T. Venumadhav, and B. Zackay, arXiv:1806.08793.

[76] D. Radice and L. Dai, Eur. Phys. J. A **55**, 50 (2019).

[77] T. Dietrich *et al.*, Phys. Rev. D **99**, 024029 (2019).